RESEARCH ARTICLE

NANO · MICRO small
www.small-journal.com

Ultrafast Carbothermal Shock Synthesis of Intermetallic Silicides with Anion-Cation Double Active Sites for Efficient Hydrogen Evolution

Tingting Liu, Yuyu Liu, Ruting Lin, Chen Chen, Zonghua Pu, Yuzhi Sun, Shengyun Huang,* Qingjun Chen, Abdullah M. Al-Enizi, Ayman Nafady, Mohd Ubaidullah, Xueqin Mu, Qiufeng Huang, and Shichun Mu**

The exploration and elucidation of the active site of catalysts is crucial for advancing the comprehension of the catalytic mechanism and propelling the development of exceptional catalysts. Herein, it is unveiled that anionic Si and cationic Pt in platinum silicide (PtSi) intermetallic compounds, obtained by ultrafast Joule heating (PtSi JH), simultaneously function as dual active sites for the hydrogen evolution reaction (HER). Density functional theory calculations reveal that, when both Pt and Si simultaneously serve as the active sites, the Gibbs free energy of hydrogen adsorption is 0.70 eV, significantly lower than that of either Pt (1.14 eV) or Si (0.90 eV) alone. Furthermore, both Pt-H and Si-H species are monitored by in situ Raman during the HER process. Consequently, PtSi JH exhibits ultralow overpotentials of 14, 30, and 51 mV at current densities of 10, 50, and 100 mA cm^{-2}, respectively, outperorming commercial Pt/C and Si powder. More importantly, the Joule heating method represents a versatile approach for synthesizing a range of metal silicides including RhSi, $RuSi_x$, and Pd_2Si. Therefore, this work opens a new avenue for the identification of genuine active sites and explores promising metal silicide for HER electrocatalysis and beyond.

1. Introduction

The escalating global energy demand, coupled with the consequential climate changes and environmental concerns, has compelled scientists to investigate sustainable and eco-friendly alternative energy sources to substitute depletable fossil fuels. In this context, the hydrogen energy exhibits significant promise. Although significant progress has been made in the hydrogen production of electrolyzed water, it necessitates the high-performance catalyst to drive the electrolyzed water, especially in acidic conditions.[1–7] Pt-based compounds are universally acknowledged as the most promising electrocatalysts for the hydrogen evolution reactions (HER) in acidic environments.[8–10] However, the extensive utilization of Pt has been significantly impeded by its exorbitant cost and low availability.[11] Therefore, the rational design and fabrication of highly efficient and cost-effective catalysts with reduced Pt amount have emerged as a paramount concern. In recent years, extensive researches have been conducted on catalysts comprising of Pt-group metals, non-noble transition metals, and non-metals, as extensively documented in the literature.[12–15] However, it is generally acknowledged that Pt still remains the predominant catalytic active sites for HER. Conversely, recent investigations have demonstrated that anionic species can also serve as catalytic active sites. For example, both theoretical and experimental evidences have supported the notion that S sites

T. Liu, Y. Liu, R. Lin, C. Chen, Z. Pu, Q. Huang
College of Chemistry & Materials Science
Fujian Normal University
Fuzhou, Fujian 350117, P. R. China
E-mail: zonghua.pu@fjnu.edu.cn

Y. Sun, S. Huang, Q. Chen
Ganjiang Innovation Academy
Key Laboratory of Rare Earths
Chinese Academy of Sciences
Ganzhou 341000, P. R. China
E-mail: shyhuang@gia.cas.cn

A. M. Al-Enizi, A. Nafady, M. Ubaidullah
Department of Chemistry
College of Science
King Saud University
Riyadh 11451, Saudi Arabia

X. Mu, S. Mu
State Key Laboratory of Advanced Technology for Materials Synthesis and Processing
Wuhan University of Technology
Wuhan 430070, P. R. China
E-mail: msc@whut.edu.cn

The ORCID identification number(s) for the author(s) of this article can be found under https://doi.org/10.1002/smll.202412528

DOI: 10.1002/smll.202412528

located at the edges of MoS_2 function as typical catalytic active sites for the HER.[16–18] Recently, Wang and co-worker demonstrated the successful transfer of the active center from the cationic Ni to the anionic S site in nickel sulfide catalyst.[19] The resulting heterogeneous NiS_2-NiS foam exhibited excellent performance toward both HER and oxygen evolution reaction. Additionally, Zhong's group provided compelling theoretical simulation and experimental results of the anionic Si site as actives for the HER.[20]

Taking inspiration from the aforementioned description, systematically designing and synthesizing a catalyst that simultaneously possesses both cationic and anionic catalytic active sites, such as Pt-Si intermetallic compounds, would likely holds great potential for achieving high electrocatalytic performance. Additionally, the acquisition of metallic silicides (MSi) still poses significant challenges due to the exceptionally high melting point of silicon (≈1687 K), rendering MSi synthesis a formidable task. Recently, despite several research groups have demonstrated the synthesis of TiSi, RuSi, LaRuSi, CeRuSi, etc. through various pyrolysis strategies such as arc-melting, strong metal reduction, and molten-salt-assisted solid-phase reduction.[21–25] On one hand, these materials were obtained either at ultrahigh temperatures (> 1300 °C) or with extended pyrolysis times (≥2 h), resulting in the formation of samples characterized by larger grain sizes and lower surface areas, consequently leading to diminished electrochemical performance. On the other hand, the ambiguity remains regarding whether both anionic Si and cationic species simultaneously serve as active sites for the HER.

On sharp contrast, Joule heating (JH), an ultrafast heating process capable of rapidly achieving ultrahigh temperatures (>3000 K) within milliseconds, has gained widespread utilization in the synthesis of high melting point nanomaterials, such as metal nitrides/carbides/dichalcogenides, ceramic materials and high-entropy-alloy nanoparticles.[26–29] The extremely short calcination time (in milliseconds to minutes) of Joule heating not only prevents the occurrence of sintering and agglomeration of active components in prolonged heat treatment, but also ensures rapid and effective dispersion of active atoms.[30] This facilitates precise regulation of the particle size, composition, and structure of the synthesized material. However, there is scarcity to synthesis of nanoscale PtSi by JH and elucidation of catalytic active sites of PtSi.

In this study, we report the synthesis of nanoscale, ordered PtSi intermetallic compounds utilizing an ultrafast JH (PtSi JH) technique. The atomic structures, electronic structures, and coordination environments of PtSi JH are elucidated through the utilization of advanced characterization techniques, including high-angle annular dark-field scanning transmission electron microscopy (HAADF-STEM) imaging and X-ray absorption fine structure (XAFS) measurements. In addition, the electrochemical measurement confirms that PtSi JH possesses an impressively low overpotential in acidic solutions, while simultaneously maintaining long-term catalytic stability. Furthermore, theoretical simulations and in situ Raman spectroscopy characterization demonstrate that both Pt and Si simultaneously act as active sites, which collectively contribute to the exceptional performance of PtSi JH toward HER. More importantly, the JH route enables the rational design of a series of intermetallic silicides (RhSi, Pd_2Si, Ru_2Si_3 and RuSi) with exceptional HER activity. Undoubtedly, the current investigation provides a significant contribution to the expanding group of intermetallic metal silicides featuring cation-anion double catalytic active sites.

2. Results and Discussion

The detailed synthesis mechanism for the ordered PtSi compounds by the Joule heating strategy is shown in **Figure 1a**. Specifically, the precursor of $PtCl_2$, SiO_2, and $NaBH_4$ were initially ground at room temperature for several minutes. Then, the obtained mixture underwent JH under an argon atmosphere. Notably, $NaBH_4$ functions as a reductant to facilitate the formation of metal silicides by decomposing to produce H_2 at high temperatures.[31] Following cooling to room temperature, the resulting sample was subjected to multiple washes with NaOH and H_2O to eliminate any byproducts, ultimately yielding the final product of PtSi JH.

The low-magnification transmission electron microscopy (TEM) image unequivocally confirms the presence of numerous PtSi JH nanoparticles (Figure 1b). The nanoparticle sizes of the PtSi JH catalysts range from 7 to 50 nm, with an average diameter of ≈20 nm (Figure S1, Supporting Information). Simultaneously, the bright-field scanning TEM (STEM) image unveil the presence of irregularly shaped PtSi JH nanoparticle (Figure 1c). The high-resolution TEM (HRTEM) image demonstrates a fringe spacing of 0.206 nm, corresponding precisely to the (121) crystal plane of orthorhombic PtSi (Figure 1d).[24] As illustrated in Figure 1e–h, the HAADF-STEM and energy-dispersive X-ray spectroscopy (EDS) elemental mapping images further demonstrate the homogeneous distribution of both Pt and Si elements within the PtSi JH nanoparticle.

The powder X-ray diffraction (XRD) peaks (**Figure 2a**) exhibit a strong correspondence with the crystal planes of PtSi (PDF# 71–0523), indicating an orthorhombic PtSi phase characterized by the Pbnm space group (Pbnm (62), $a_0 = 5.916$ Å, $b_0 = 5.577$ Å, $c_0 = 3.587$ Å, Figure S2, Supporting Information).[27] Furthermore, the XAFS measurements were conducted to gain a comprehensive understanding of the electronic state of PtSi JH. The X-ray absorption near-edge structure (XANES) at the Pt L_3-edge is presented in Figure 2b, providing a comparative reference with Pt foil and PtO_2. The white-line (WL) intensity of PtSi JH is observed to exceed that of Pt foil, yet it remains significantly lower than that of PtO_2, indicating an oxidation state of $Pt^{\delta+}$ ($0 < \delta^+ < 4$).[32,33] Additionally, the Fourier transform extended X-ray absorption fine structure (FT-EXAFS) spectra of PtO_2 and Pt foil revealed distinct peaks at 1.62 and 2.62 Å, corresponding to the coordination of Pt—O and Pt—Pt bond, respectively. In contrast, the FT-EXAFS spectra of PtSi JH exhibit a prominent peak at 1.95 Å, which can be assigned to the presence of a Pt—Si bond (Figure 2c).[24] The k-space exhibits smooth oscillates without large peaks, indicating the presence of more plausible data (Figure S3, Supporting Information).[34] Moreover, the information is further intuitively visualized through wavelet transform (WT)-EXAFS analysis (Figure 2e-g). The wavelet data near 5.2 $Å^{-1}$ of PtSi JH represents the Pt-Si signal, which is distinct from both the Pt-Pt signal (10.1 $Å^{-1}$) and the Pt-O signal (6.2 $Å^{-1}$) observed in Pt foil and in PtO_2, respectively.[35] Similarly, the Si K-edge XANES spectra for PtSi JH and the reference samples (SiO_2 and Si) are shown in Figure 2d. The Si K-edge XANES peak of PtSi JH shows a

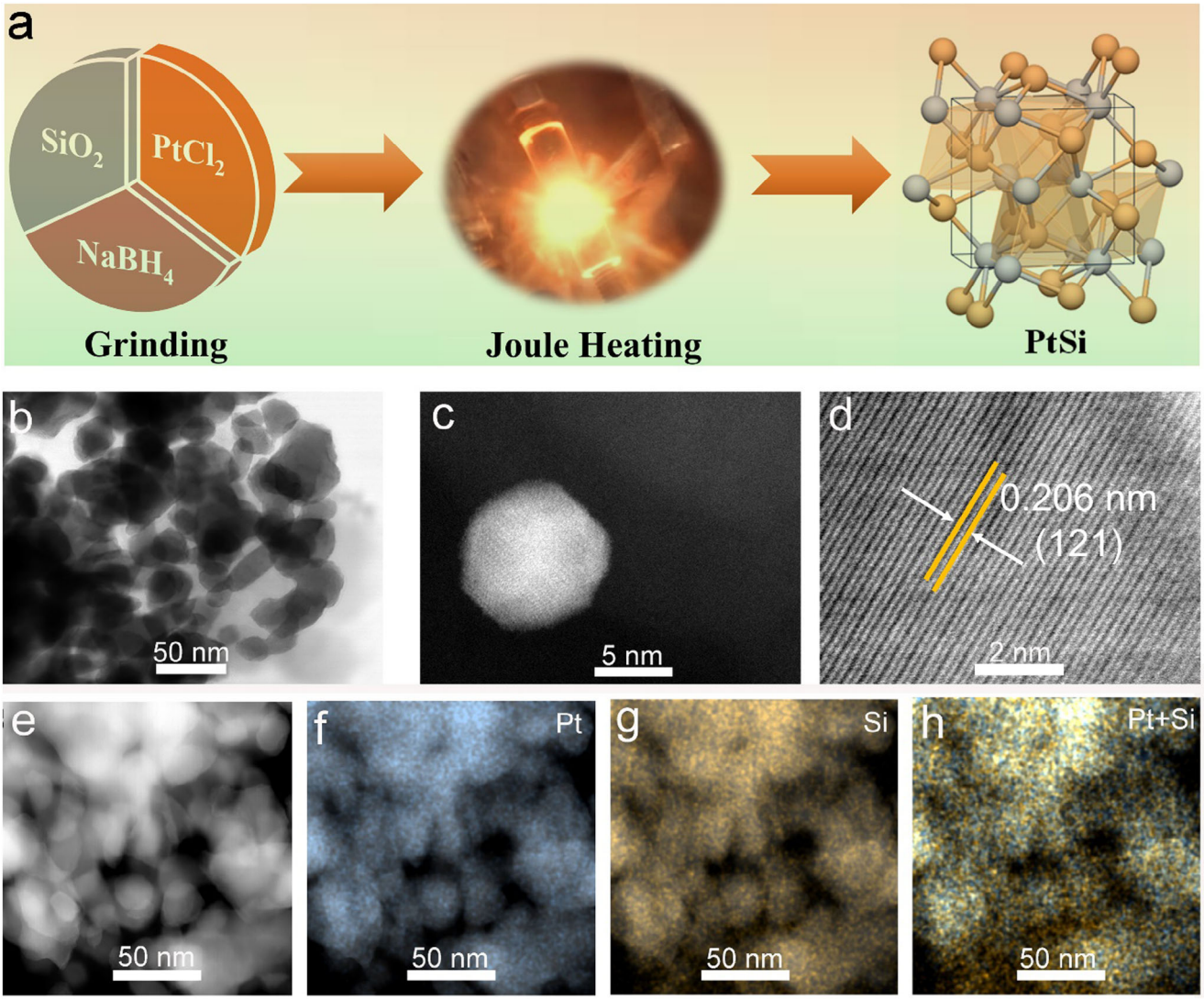

Figure 1. a) Schematic of the synthesis process of PtSi nanoparticles via Joule heating. b) TEM, c) bright-field (BF) STEM, and d) HRTEM images of PtSi JH. e) STEM-HAADF image and corresponding STEM-EDS elemental mapping of PtSi JH nanoparticles. f) Pt (blue), g) silicon (yellow), and h) combined Pt and Si maps.

significant shift toward lower binding energy compared to that of Si.[36] These findings provide evidence for the negative charge on Si atoms in PtSi, indicating electron transfer from the Pt atom to the Si atom. Furthermore, the elementary composition of PtSi was characterized using X-ray photoelectron spectroscopy (XPS). As illustrated in Figure S4a (Supporting Information), the results indicate that the PtSi JH is predominantly composed of Pt, Si, B, C, and O. The presence of elemental C and O can be attributed to the absorption of CO_2, H_2O, or O_2 to minor surface oxidation of PtSi JH potentially caused by exposure to air. The presence of B can be attributed to the utilization of sodium borohydride as a reducing agent during the material synthesis process. Specifically, the B 1s spectrum of PtSi JH shows two peaks at ≈186.9 and ≈188.3 eV, which are indicative of the Pt—B bond, while the peak at ≈192.1 eV is associated with the B—O bond (Figure S4b, Supporting Information).[37] This XPS characterization results suggest the incorporation of boron doping into the interstices of the PtSi JH. Notably, it is reported that B doping may further activate the materials, thereby enhancing the absorption of H_2O and consequently boosting the HER catalytic activity.[38] In a word, all the characterizations unequivocally validate the formation of a distinct PtSi phase, which is characteristic of intermetallic compounds.

The HER performance of the PtSi JH was examined in 0.5 M H_2SO_4 electrolytes, with all potentials calibrated using a reversible hydrogen electrode (RHE) as the reference standard. Before conducting the HER tests, the PtSi JH compound was activated through performing a series of linear sweep voltammetry (LSV) scans ranging from 0 to −0.5 V versus saturated calomel electrode (SCE). For comparison, commercial Pt/C and Si particles were also assessed under identical experimental conditions. **Figure 3a** reveals the polarization curves for the HER over PtSi JH, commercial Pt/C, and Si. All LSVs measurements were conducted with *iR*-compensation, wherein the internal

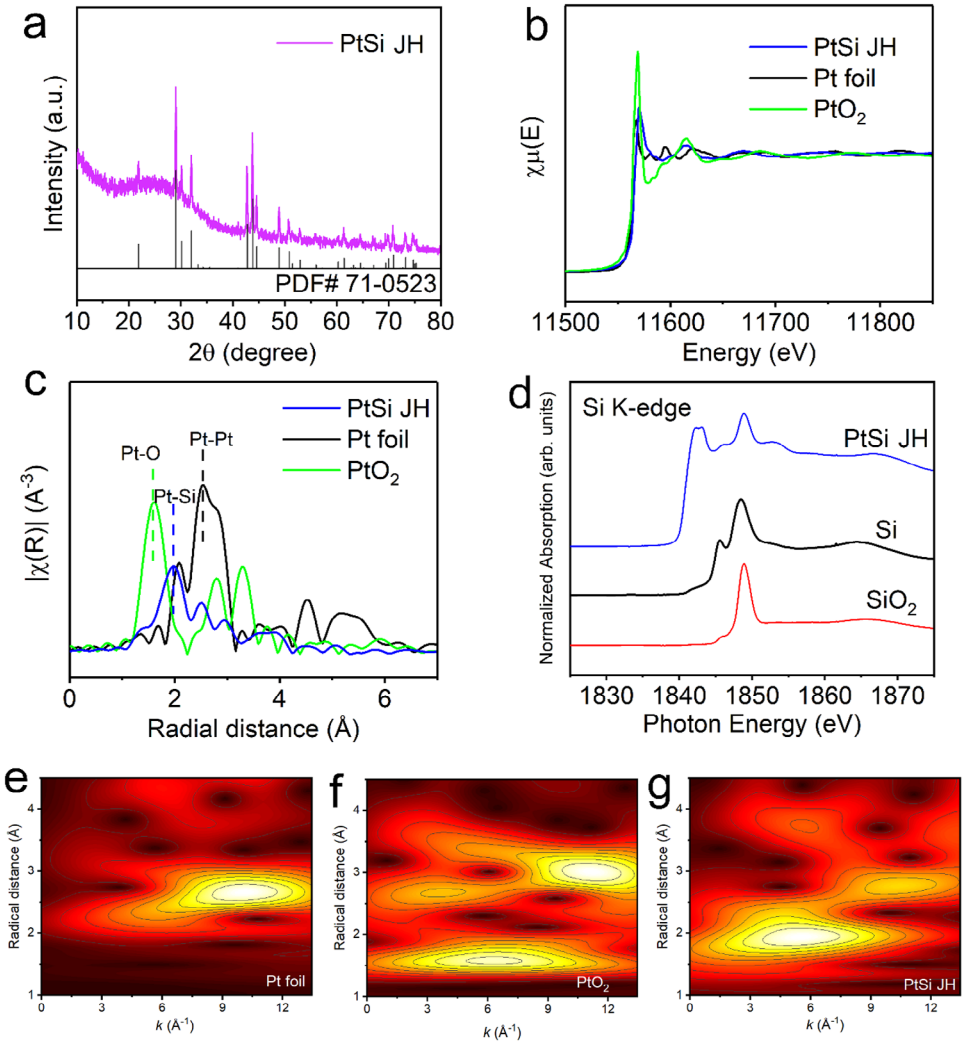

Figure 2. a) XRD pattern of PtSi JH. b) The normalized XANES spectra at the Pt L3-edge for the PtSi JH, PtO_2, and Pt foil. c) Corresponding Fourier transforms (FT) of the EXAFS spectra of PtSi JH, PtO_2, and Pt foil. d) XANES spectra for SiO_2, Si, and PtSi JH at Si K-edge. Wavelet transform of EXAFS spectra at Pt L3-edge, e) Pt foil, f) PtO_2, and g) PtSi JH.

resistance was determined using electrochemical impedance spectroscopy (EIS) (Figure S5, Supporting Information). As illustrated in Figure 3a, the Si is inactive for HER, while in sharp contrast, both commercial Pt/C and PtSi JH show remarkable catalytic activity toward HER with a near zero millivolt onset potential. In particular, PtSi JH needs the overpotentials of 14, 30, and 51 mV at current densities of 10, 50, and 100 mA cm^{-2}, respectively, surpassing the performance of commercial Pt/C catalysts (14, 44, and 78 mV) (Figure 3b). Moreover, the PtSi JH catalyst exhibits a significantly higher HER activity compared to other Pt-group metal-based catalysts reported in acidic electrolytes (Figure 3d; Table S1, Supporting Information).[24,25,39,40] As illustrated in Figure 3c, the outstanding HER performance of PtSi JH is further demonstrated by a low Tafel slope (≈23.2 mV dec^{-1}), slightly lower than that of commercial Pt/C (≈26.4 mV dec^{-1}).

In addition to the excellent catalytic activity, the HER durability of PtSi JH was further investigated. As depicted in Figure 3e, the LSV curves of PtSi JH reveal negligible degradation even after undergoing 2000 CV cycles. Furthermore, as shown in Figure 3f, the current density of PtSi JH remains virtually unchanged in acidic electrolyte following continuous electrolysis for a duration of 24 h, thereby providing additional evidence to support the exceptional stability exhibited by PtSi JH. Moreover, the XRD analysis of fresh and post-HER PtSi JH catalysts (Figure S6, Supporting Information) further present the preservation of intermetallic PtSi in terms of composition, thereby indicating its exceptional durability toward HER in a 0.5 M H_2SO_4 electrolytes. More importantly, PtSi JH exhibits a Faradaic efficiency (FE) exceeding 97% during the HER (Figures S7–S9, Supporting Information), implying that the observed current can predominantly be attributed to the electrocatalysis process of HER. Undoubtedly, these analyses unequivocally demonstrate that PtSi JH possesses remarkable and enduring HER catalytic performance.

To elucidate the exceptional HER activity of PtSi JH, theoretical simulations and in situ Raman characterization techniques were

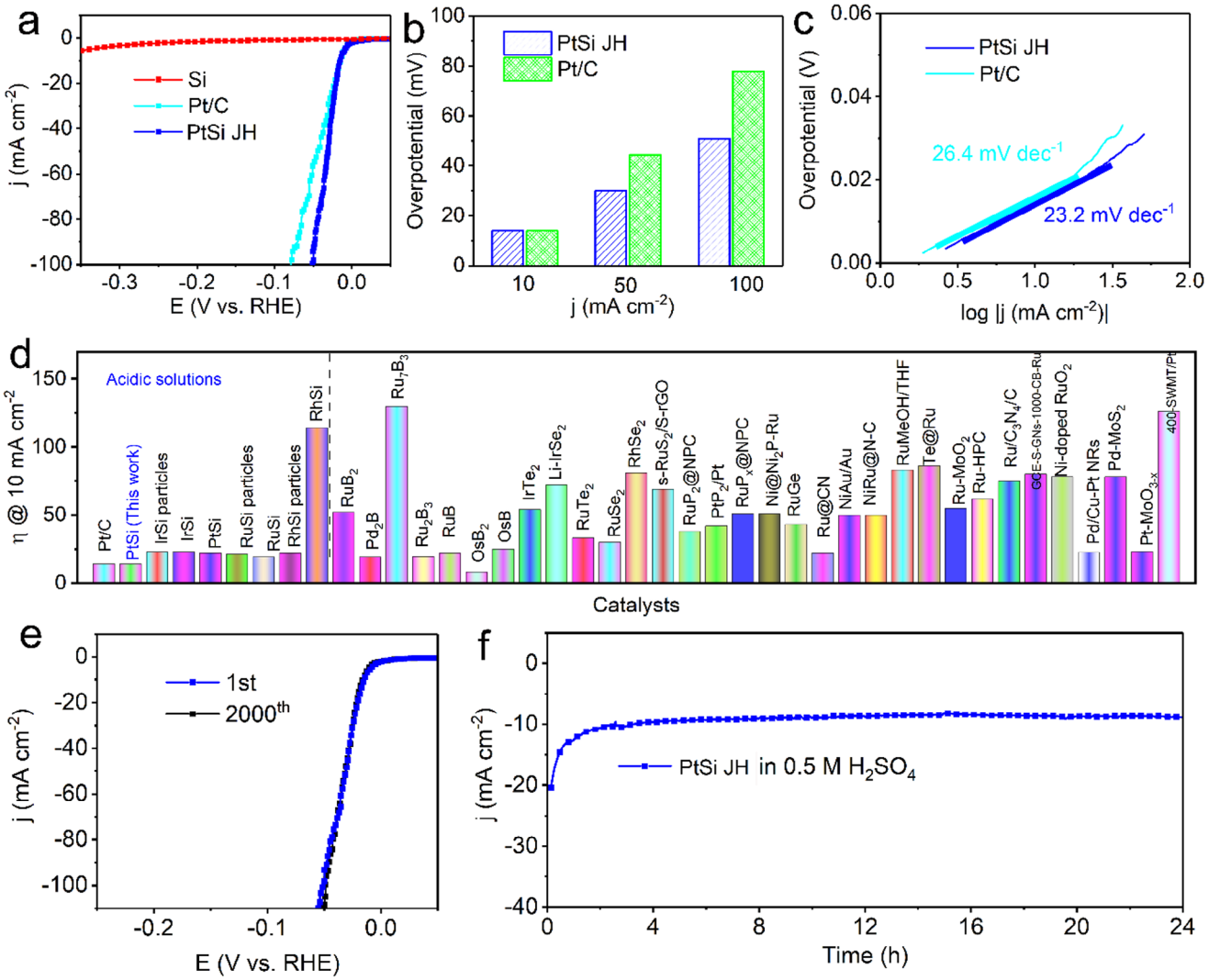

Figure 3. a) The LSV curves for PtSi JH, commercial Pt/C, and Si in 0.5 M H_2SO_4. b) Overpotentials for PtSi JH and commercial Pt/C materials at j = 10, 50, and 100 mA cm^{-2}. c) Tafel plots for PtSi JH and Pt/C in 0.5 M H_2SO_4. d) Comparison of the overpotentials at 10 mA cm^{-2} with recently reported HER materials in acidic solution. e) LSV curves were recorded before and after 2000 CV cycles for PtSi JH. f) HER durability of PtSi JH in 0.5 M H_2SO_4 at constant potentials for 24 h.

conducted. The ideal HER catalyst should possess a adsorption free energy of atomic hydrogen (ΔG_{H^*}) approaching zero, ensuring consistent hydrogen adsorption and desorption.[41,42] Herein, we considered three distinct scenarios as the models for density functional theory (DFT) calculations. One scenario involves either Pt or Si sites as the active sites for H adsorption, while the other scenario considers both Pt and Si atoms simultaneously act as H adsorption sites. Specifically, **Figure** 4a–c illustrates the models used for DFT calculations. As illustrated in Figure 4d, when both Pt and Si atoms function simultaneously as active sites, the calculated ΔG_{H^*} value is 0.70 eV, obviously lower than the individual H adsorption energy on either Pt sites (1.14 eV) or Si sites (0.90 eV). In other words, this suggests that both anionic Si and cationic Pt act as real active sites during the HER process. Moreover, Figure 4e demonstrates a conspicuous electron rearrangement according to the Bader charge analysis, indicating an active electronic interaction between Pt and Si atoms. Furthermore, we conducted an analysis on the projected density of states (PDOS) of PtSi and Pt. The obtained results can be elucidated using a d-band model due to the correlation between the adsorption energy of the adsorbate and the d-band center.[43] The calculated d-band centers for PtSi and Pt are 2.43 and 2.93 eV, respectively. It is widely acknowledged that a higher d-band energy corresponds to stronger adsorption.[44] In other words, after the ordered filling of Si atoms in Pt lattices, the ordered Pt-Si compounds exhibit a modest ability toward hydrogen adsorption and desorption, and therefore, benefiting from the HER. More significantly, in situ Raman spectroscopy characterization further confirms that both Pt and Si atoms within PtSi JH serve as the primary adsorption sites for HER. As shown in Figure 4g, as the potential decreases from −10 to −20 mV, two distinct peaks emerge at ≈2100 and ≈2004 cm^{-1}. These peaks are attributed to the vibrational modes of Pt—H bond and the stretching vibrations of the Si—H bond,[20,45] respectively. These results validate

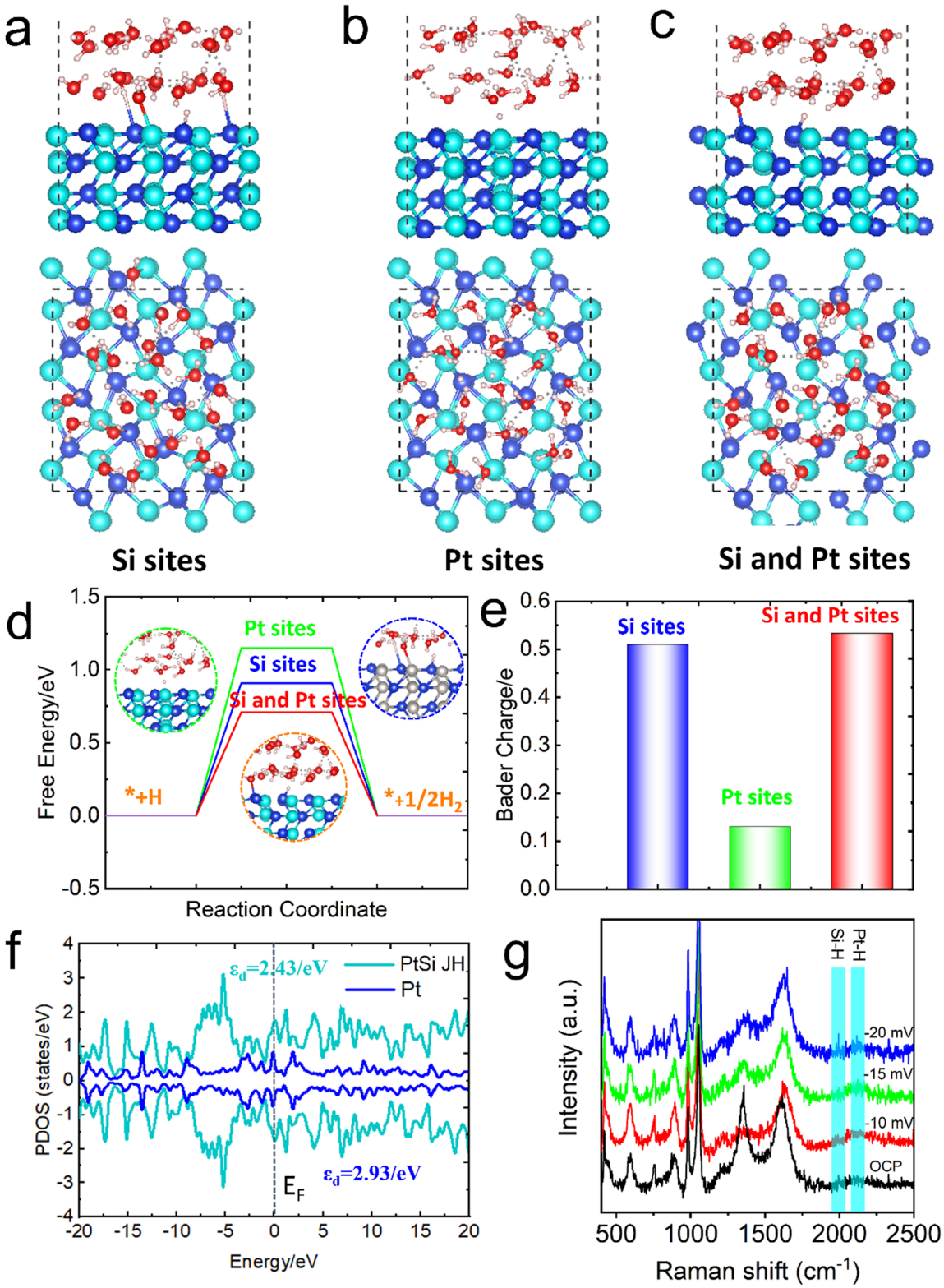

Figure 4. a–c) Theoretical model used in DFT calculation. d) Calculated free-energy diagram of HER at equilibrium potential for PtSi JH with different active sites. e) Bader charge analysis for PtSi JH with different active sites. f) Calculated PDOS for the d orbital of Pt and PtSi JH. g) In situ Raman spectra of PtSi JH collected at HER condition.

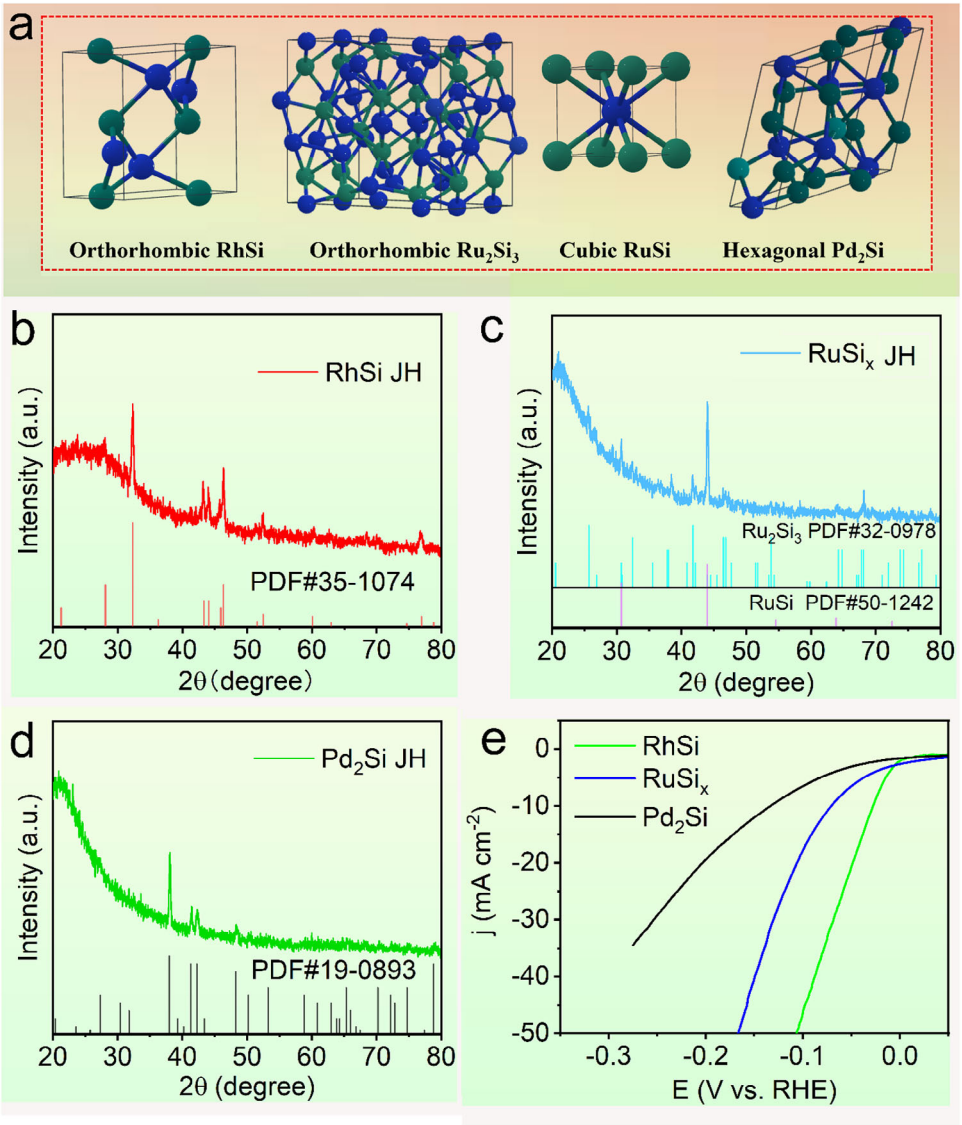

Figure 5. a) The crystal structures of RhSi, Ru_2Si_3, RuSi, and Pd_2Si. XRD patterns of b) RhSi, c) RuSix, and d) Pd_2Si. e) HER performances of RhSi, RuSix, and Pd_2Si in 0.5 m H_2SO_4 solutions.

that both Pt and Si sites act as the real catalytic active sites for HER.

It is important to note that this JH technology for the synthesis of PtSi was also effective in preparing other noble-metal-based intermetallic silicides. For example, RhSi, Pd_2Si, and $RuSi_x$ (with both Ru_2Si_3 and RuSi phases) have been obtained when replacing the metal precursors using $RhCl_3$, $PdCl_2$, and $RuCl_3$ by a similar strategy (the detailed experimental parameters are provided in Table S2, Supporting Information). **Figure 5a** shows the typical structures of RhSi, Ru_2Si_3, RuSi and Pd_2Si intermetallic phases. Remarkably, powder XRD results suggest that pure RhSi (PDF #35-1074) with orthorhombic phase and Pd_2Si with hexagonal phase (PDF #19-0893) have been obtained, while the XRD pattern for $RuSi_x$ can be ascribed to the hybrids of Ru_2Si_3 (PDF #32-0978) with orthorhombic phase and RuSi (PDF #50-1242) with cubic phase (Figure 5b–d).[25] These results demonstrated that the JH strategy can be used to synthesize a family of metal-based intermetallic silicides (RhSi, Ru_2Si_3, RuSi, and Pd_2Si, etc.). More importantly, as illustrated in Figure 5e, RhSi, Pd_2Si, and $RuSi_x$ further exhibit good HER performance with overpotential of 27, 70, and 132 mV to achieve a current density of 10 mA cm^{-2} under acidic solutions, respectively. All of these results are further demonstrating the generality of the flash JH process.

3. Conclusion

In summary, the ordered Pt-Si intermetallic compounds have been fabricated by flash Joule heating. The obtained PtSi JH exhibit exceptional electrocatalytic activity and remarkable stability toward HER. In acidic media, operationally relevant current densities of 10, 50, and 100 mA cm^{-2} can be achieved with

overpotentials as low as 14, 30, and 51 mV, respectively. At the same time, the exceptional stability under acidic conditions attests to the practicality of PtSi JH. DFT calculation reveals that the optimal value of ΔG_{H^*} can be achieved when both Pt and Si simultaneously serving as the active sites. More importantly, in situ Raman spectroscopy characterization further confirms the Pt and Si double actives within PtSi JH as primary adsorption sites for HER. Undoubtedly, the excellent performance exhibited by the ordered Pt-Si intermetallic compounds paves a pathway for the design of high-performance catalysts synthesized by JH.

4. Experimental Section

Synthesis of PtSi: 56 mg of $PtCl_2$, 16 mg SiO_2, and 18 mg of $NaBH_4$ were mixed and ground into a fine powder. Subsequently, the above precursor mixture was subjected to JH (current ≈90 A, potential ≈40 V, thermal shock time ≈15 s) under Ar flow. After cooling, the black powder underwent three successive washes with sodium hydroxide and deionized water to effectively eliminate any residual by-products.

Preparation of the Working Electrode: The homogeneous ink was prepared by sonicating a mixture of 5.0 mg PtSi, 1.0 mg carbon black, 440 µL isopropyl ethanol, 220 µL water, and 10 µL 5 wt.% Nafion for 1 h. The working electrode was fabricated by depositing of 7.5 µL catalyst-ink solution onto a glassy carbon electrode (GCE), followed by rotation at 600 rpm for at least minimum of 30 min under ambient conditions, resulting in a loading weight: 0.7 mg cm^{-2}).

Materials Characterization: The crystal structures were collected by XRD equipped with a Cu Kα radiation source. The TEM measurements were conducted using a HITACHI H-8100 electron microscopy operating at an accelerating voltage of 200 kV. XAS data were collected on the 06ID-1 Hard X-ray Micro Analysis (HXMA) beamline at the Canadian Light Source. The spectra were first normalized by subtracting the pre-edge and post-edge backgrounds, followed by normalization with respect to the edge height. Subsequently, the data was transformed from energy space to k space using ATHENA software.

Electrochemical Measurements: The catalytic activity and stability were assessed using a standard three-electrode cell at ambient temperature (≈298K). The working electrode was a GCE (diameter: 3 mm) or a carbon paper (0.5 × 0.5 cm^2). The reference and counter electrode were comprised of an SCE and graphite plate, respectively. The polarization data were acquired in 0.5 M H_2SO_4 media with a scanning rate of 5 mV s^{-1}. All the potentials were calibrated against the RHE. All the polarization curves were obtained with correction from ohmic potential drop (*iR*), which accounts for solution resistance. EIS measurements were carried out at the same potential value with the frequency ranging from 10^5 to 1 Hz under a voltage of 5 mV, and the impedance spectra were presented in the form of a Nyquist plot. The *iR*-corrected potential was determined by incorporating the internal resistance correction obtained from EIS, utilizing the following Equation:

$$\text{Eactual} = \text{Etest} - \text{iR} \times 100\% \quad (1)$$

where E_{test}, *i and R* represent the initial potential, corresponding current, and internal resistance, respectively. E_{actual} refers to the potential adjusted for the effects of *iR*.

The FE was determined by experimentally measuring the amount of H_2 produced and comparing it to the theoretically expected yield, quantifying the extent of agreement between experimental and theoretical values. The water drainage technique was utilized for the collection of the generated H_2. The electrode was subjected to a constant potential while the concurrent measurement of evolved gas volume was conducted. Then, the moles of H_2 were determined using gas laws, followed by the calculation of the theoretically anticipated quantity of hydrogen gas by applying Faraday's law. This law states that 96 485 C passing through the system causes 1 equivalent of reaction.

Supporting Information

Supporting Information is available from the Wiley Online Library or from the author.

Acknowledgements

This work was supported by the National Natural Science Foundation of China (Grant No. 22402030; 22379117), the Fujian Province Young and Middle-Aged Teacher Education Research Project (JZ240012; JZ230009), the Youth Innovation Promotion Association of Chinese Academy of Sciences (2023341) and the Jiangxi Provincial Natural Science Foundation (20232BAB204101). The authors extend their sincere appreciation to the Researchers Supporting Project number (RSPD2025R55), King Saud University, Riyadh, Saudi Arabia for the support.

Conflict of Interest

The authors declare no conflict of interest.

Data Availability Statement

The data that support the findings of this study are available from the corresponding author upon reasonable request.

Keywords

active sites, DFT calculation, hydrogen evolution reaction, intermetallic metal silicides, joule heating

Received: December 22, 2024
Revised: March 6, 2025
Published online:

[1] J. A. Turner, *Science* **2004**, *305*, 972.
[2] J. He, L. Cao, J. Cui, G. Fu, R. Jiang, X. Xu, C. Guan, *Adv. Mater.* **2024**, *36*, 2306090.
[3] Z. W. Seh, J. Kibsgaard, C. F. Dickens, I. Chorkendorff, J. K. Nørskov, T. F. Jaramillo, *Science* **2017**, *355*, 4998.
[4] J. H. Montoya, L. C. Seitz, P. Chakthranont, A. Vojvodic, T. F. Jaramillo, J. K. Nørskov, *Nat. Mater.* **2017**, *16*, 70.
[5] Y. Zhao, L. Zhang, J. Liu, K. Adair, F. Zhao, T. Wu, X. Bi, K. Amine, J. Lu, X. Sun, *Chem. Soc. Rev.* **2021**, *50*, 3889.
[6] D. Chen, T. Liu, P. Wang, J. Zhao, C. Zhang, R. Cheng, W. Li, P. Ji, Z. Pu, S. Mu, *ACS Energy Lett.* **2020**, *5*, 2909.
[7] H. Wu, C. Feng, L. Zhang, J. Zhang, D. P. Wilkinson, *Electrochem. Energy Rev.* **2021**, *4*, 473.
[8] C. Seitz, C. F. Dickens, K. Nishio, Y. Hikita, J. Montoya, A. Doyle, C. Kirk, A. Vojvodic, H. Y. Hwang, J. K. Norskov, T. F. Jaramillo, *Science* **2016**, *353*, 1011.
[9] M. Blasco-Ahicart, J. Soriano-Lpez, J. J. Carb, J. M. Poblet, J. Galan-Mascaros, *Nat. Chem.* **2018**, *10*, 24.
[10] Z. Pu, G. Zhang, A. Hassanpour, D. Zheng, S. Wang, S. Liao, Z. Chen, S. Sun, *Appl. Energy* **2021**, *283*, 116376.
[11] Y. Mu, T. Wang, J. Zhang, C. Meng, Y. Zhang, Z. Kou, *Electrochem. Energy Rev.* **2021**, *5*, 145.
[12] W. Liu, X. Wang, F. Wang, K. Du, Z. Zhang, Y. Guo, H. Yin, D. Wang, *Nat. Commun.* **2021**, *12*, 6776.
[13] Y. Li, S. Li, A. Nagarajan, Z. Liu, S. Nevins, Y. Song, G. Mpourmpakis, R. Jin, *J. Am. Chem. Soc.* **2021**, *143*, 11102.

[14] Z. Lin, B. Xiao, M. Huang, L. Yan, Z. Wang, Y. Huang, S. Shen, Q. Zhang, L. Gu, W. Zhong, *Adv. Energy Mater.* **2022**, *12*, 2200855.
[15] W. Zhang, N. Han, J. Luo, X. Han, S. Feng, W. Guo, S. Xie, Z. Zhou, P. Subramanian, K. Wan, J. Arbiol, C. Zhang, S. Liu, M. Xu, X. Zhang, J. Fransaer, *Small* **2022**, *18*, 2103561.
[16] B. Hinnemann, P. G. Moses, J. Bonde, K. P. Jørgensen, J. H. Nielsen, S. Horch, I. Chorkendorff, J. K. Nørskov, *J. Am. Chem. Soc.* **2005**, *127*, 5308.
[17] T. F. Jaramillo, K. P. Jørgensen, J. Bonde, J. H. Nielsen, S. Horch, I. Chorkendorff, *Science* **2007**, *317*, 100.
[18] J. Chen, G. Liu, Y. Z. Zhu, M. Su, P. Yin, X. Wu, Q. Lu, C. Tan, M. Zhao, Z. Liu, W. Yang, H. Li, G. Nam, L. Zhang, Z. Chen, X. Huang, P. Radjenovic, W. Huang, Z. Tian, J. Li, H. Zhang, *J. Am. Chem. Soc.* **2020**, *142*, 7161.
[19] P. Wang, T. Wang, R. Qin, Z. Pu, C. Zhang, J. Zhu, D. Chen, D. Feng, Z. Kou, S. Mu, J. Wang, *Adv. Energy Mater.* **2022**, *12*, 2103359.
[20] S. Shen, Z. Hu, H. Zhang, K. Song, Z. Wang, Z. Lin, Q. Zhang, L. Gu, W. Zhong, *Angew. Chem., Int. Ed.* **2022**, *61*, 202206460.
[21] Y. He, T. Wang, M. Zhang, T. Wang, L. Wu, L. Zeng, X. Wang, M. Boubeche, S. Wang, K. Yan, S. Lin, H. Luo, *Small* **2021**, *17*, 2006153.
[22] W. Cai, C. Zhou, X. Hu, T. Jiao, Y. Liu, L. Li, M. Kitano, H. Hosono, J. Wu, *ACS Catal.* **2023**, *13*, 4752.
[23] H. Chen, M. Zhang, K. Zhang, Z. Li, X. Liang, X. Ai, X. Zou, *Small* **2022**, *18*, 2107371.
[24] Z. Pu, T. Liu, G. Zhang, Z. Chen, D. Li, N. Chen, W. Chen, Z. Chen, S. Sun, *Adv. Energy Mater* **2022**, *12*, 2200293.
[25] D. Chen, Z. Pu, P. Wang, R. Lu, W. Zeng, D. Wu, Y. Yao, J. Zhu, J. Yu, P. Ji, S. Mu, *ACS Catal.* **2022**, *12*, 2623.
[26] W. Ping, C. Wang, R. Wang, Q. Dong, Z. Lin, A. H. Brozena, J. Dai, J. Luo, L. Hu, *Sci. Adv.* **2020**, *6*, eabc8641.
[27] A. Taibi, E. Gil-González, P. E. Sánchez-Jiménez, A. Perejón, L. A. Pérez-Maqueda, *Cerm. Int.* **2025**, *51*, 5483.
[28] H. Wu, Q. Lu, Y. Li, J. Wang, Y. Li, R. Jiang, J. Zhang, X. Zheng, X. Han, N. Zhao, J. Li, Y. Deng, W. Hu, *Nano Lett.* **2022**, *22*, 6492.
[29] C. Choi, J. Shin, L. Eddy, V. Granja, K. M. Wyss, B. Damasceno, H. Guo, G. Gao, Y. Zhao, C. Fred Higgs III, Y. Han, J. M. Tour, *Nat. Chem.* **2024**, *16*, 1831.
[30] B. Deng, Z. Wang, W. Chen, J. Li, D. Luong, R. A. Carter, G. Gao, B. I. Yakobson, Y. Zhao, J. M. Tour, *Nat. Commun.* **2022**, *13*, 262.
[31] D. M. F. Santos, C. A. C. Sequeira, *Renew. Sustain. Energy Rev.* **2011**, *15*, 3980.
[32] T. Liu, Z. Pu, Z. Chen, M. Wu, Y. Xia, S. Liu, N. Chen, W. Chen, L. Zhang, Z. Chen, G. Zhang, S. Sun, *Susmat* **2024**, *4*, e246.
[33] W. Guo, L. Cheng, X. Gao, J. Xu, C. Chen, P. Liu, D. He, L. Tian, J. Song, H. Zhou, Y. Wu, *ACS Catal.* **2023**, *13*, 5397.
[34] M. Henstridge, C. Pfeiffer, D. Wang, A. Boltasseva, V. M. Shalaev, A. Grbic, R. Merlin, *Science* **2018**, *362*, 439.
[35] Y. Chen, P. Wang, H. Hao, J. Hong, H. Li, S. Ji, A. Li, R. Gao, J. Dong, X. Han, M. Liang, D. Wang, Y. Li, *J. Am. Chem. Soc.* **2021**, *143*, 18643.
[36] R. Sammynaiken, S. J. Naftel, T. K. Sham, K. W. Cheah, B. Averboukh, R. Huber, Y. Shen, G. Qin, Z. Ma, W. Zong, *J. Appl. Phys.* **2002**, *92*, 3000.
[37] T. Liu, Z. Chen, S. Liu, P. Wang, Z. Pu, G. Zhang, S. Sun, *Angew. Chem., Int. Ed.* **2025**, *64*, 202414021.
[38] Q. Yu, Y. Fu, J. Zhao, B. Li, X. Wang, X. Liu, L. Wang, *Appl. Catal. B: Environ.* **2023**, *324*, 122297.
[39] H. Zhang, K. Song, Z. Lin, Z. Wang, L. Zhang, S. Shen, L. Gu, W. Zhong, *Adv. Funct. Mater.* **2024**, *36*, 2405897.
[40] W. Cai, X. He, T. Ye, X. Hu, C. Liu, M. Sasase, M. Kitano, T. Kamiya, H. Hosono, J. Wu, *Small* **2024**, *20*, 2402357.
[41] D. Chen, R. Lu, R. Yu, H. Zhao, D. Wu, Y. Yao, K. Yu, J. Zhu, P. Ji, Z. Pu, Z. Kou, J. Yu, J. Wu, S. Mu, *Nano-Micro Lett.* **2023**, *15*, 168.
[42] T. Liu, J. Wang, C. Zhong, S. Lu, W. Yang, J. Liu, W. Hu, C. Li, *Chem. - Eur. J.* **2015**, *29*, 7826.
[43] B. Hammer, J. K. Nørskov, *Adv. Catal.* **2000**, *45*, 71.
[44] A. Ruban, B. Hammer, P. Stoltze, H. L. Skriver, J. K. Nørskov, *J. Mol. Catal. A* **1997**, *115*, 421.
[45] A. Haryanto, K. Jung, C. Lee, D. Kim, *J. Energy Chem.* **2024**, *90*, 632.